Preprint, published as: Atharv Jog and Daniel Gall, "Resistivity size effect in epitaxial iridium layers," J. Appl. Phys. **130**, 115103 (2021); https://doi.org/10.1063/5.0060845

Resistivity size effect in epitaxial iridium layers

Atharv Jog and Daniel Gall [a)]

Department of Materials Science and Engineering, Rensselaer Polytechnic Institute, 110 8th St, Troy, NY 12180, USA

[a)]Author to whom correspondence should be addressed: galld@rpi.edu

The resistivity size effect in Ir is quantified with *in situ* and *ex situ* transport measurements at 295 and 77 K using epitaxial layers with thickness $d = 5 – 140$ nm deposited on MgO(001) and Al_2O_3(0001) substrates. Data fitting with the Fuchs-Sondheimer model of the measured resistivity ρ vs d for single-crystal Ir(001)/MgO(001) layers deposited at T_s = 1000 °C yields an effective electron mean free path $\lambda_{eff} = 7.4 \pm 1.2$ nm at 295 K, a room-temperature bulk resistivity $\rho_o = 5.2$ μΩcm, and a temperature independent product $\rho_o\lambda_{eff} = (3.8 \pm 0.6)\times10^{-16}$ Ωm^2 which is in good agreement with first-principles predictions. Layers deposited at $T_s = 700$ °C and stepwise annealed to 1000 °C exhibit a unique polycrystalline multi-domain microstructure with smooth renucleated 111-oriented grains that are >10 μm wide for d = 10 nm, resulting in a 26% lower $\rho_o\lambda_{eff}$. Ir(111)/Al_2O_3(0001) layers exhibit two 60°-rotated epitaxial domains with an average lateral grain size of 88 nm. The grain boundaries cause a thickness-independent resistivity contribution $\Delta\rho_{gb} = 0.86 \pm 0.19$ and 0.84 ± 0.12 μΩcm at 295 K and 77 K, indicating an electron reflection coefficient $R = 0.52 \pm 0.02$ for this boundary characterized by a 60° rotation about the <111> axis. The overall results indicate that microstructural features including strain fields from misfit dislocations and/or atomic level roughness strongly affect the resistivity size effect in Ir. The measured $\rho_o\lambda_{eff}$ for Ir is smaller than for any other elemental metal and 69%, 43%, and 25% below reported $\rho_o\lambda$ products for Co, Cu, and Ru, indicating that Ir is a promising alternate metal for narrow high-conductivity interconnects.

I. INTRODUCTION

The resistivity increase of a metal wire with decreasing cross-section[1,2] is referred to as the resistivity size effect[3,4] and represents a major challenge for the continued downscaling of integrated circuits[5] because of the resulting increased signal delay and power consumption in interconnect lines. The resistivity size effect is primarily due to electron scattering at surfaces[6–10] and grain boundaries[11–16] which are affected by the surface chemistry and structure[8,14,17–21] and the relative grain orientations.[2,11,16,22–25] The semiclassical Fuchs and Sondheimer[26,27] and Mayadas and Shatzkes[28] models use the phenomenological surface scattering specularity parameter p and the grain boundary reflection coefficient R to describe electron scattering at surfaces and grain boundaries and predict an overall resistivity increase that is proportional to $\rho_o\lambda/d$, where $\rho_o\lambda$ is the product of the bulk resistivity times the bulk electron-phonon scattering mean free path, and d is the distance between scattering interfaces, that is the width of the conductor or the average grain size.[29] We note that these classical-models deviate from the quantum mechanical descriptions[30–33] and diverge from experimental measurements for narrow (< 10 nm) conductors.[34–37] Nevertheless, they are useful in the search for metals for narrow interconnects as they provide a single performance metric, the $\rho_o\times\lambda$ product, which promises a low resistivity in the limit of narrow wires.[38,39]

Iridium has a predicted $\rho_o\lambda = 3.69\times10^{-16}$ Ωm^2 which is 45%, 50%, 55%, and 28% smaller than the corresponding predictions for Cu, Co, W and Ru, respectively,[39] suggesting its potential

to outperform competing metal solutions in highly scaled interconnect lines. In addition, the high melting point and the reported stability of Ir films on SiO_2 lead to a superior electromigration resistance with the potential for barrierless metallization[40] which provides a considerable conductance benefit.[9,41] The predicted low $\rho_o\lambda$ product is, however, no guarantee for a small resistivity scaling, since the calculated $\rho_o\lambda$ agrees well with experiments only for some metals including Ru(0001),[42,43] Cu(001),[8] and Ag(001)[13] but disagrees with the measured resistivity vs thickness for epitaxial Rh(001),[44] Co(0001),[9,37] W(001),[45] W(011),[45] Nb(001) and Nb(011),[46] and Ni(001)[47] where $\rho_o\lambda$ values are 39%, 67%, 72%, 68%, 293-743%, and 349% larger than predicted from first principles. Thus, experiments that directly quantify the resistivity size effect in Ir are required to confirm or correct the theoretical prediction. A previous investigation using polycrystalline Ir/SiO_2 layers found a relatively small resistivity size effect with a 71% increase in ρ with decreasing d = 31 to 3 nm.[15] Their data fitting, using λ = 8.1 nm, yields a grain boundary reflection coefficient R = 0.47 and nearly specular surface scattering (p > 0.9). However, λ is not uniquely defined by the measured data which can also be described by other combinations of λ, R and p values. This challenge motivates our study on the measurement of the resistivity scaling in epitaxial Ir layers where confounding effects from grain boundary scattering are absent.

In this paper, we experimentally determine λ and the $\rho_o\lambda$ product for Ir from measurements of the thickness dependent resistivity of epitaxial Ir(001) and Ir(111) layers which are sputter deposited on single-crystal MgO(001) and Al_2O_3(0001) substrates. The growth of single-crystal Ir(001)/MgO(001) layers which have a high crystalline quality, low surface roughness, and are thin but continuous is quite challenging: (i) growth at T_s = 1000 °C results in a high crystalline quality but a large roughness or even a discontinuous microstructure if the thickness is reduced to d = 11.5 and 7.7 nm, (ii) a lower T_s = 700 °C leads to continuous layers, however, with a lower crystalline quality, and (iii) growth at T_s = 700 °C followed by stepwise *in situ* annealing to 1000 °C results in a multi-domain polycrystalline microstructure which is attributed to renucleation into 111-oriented grains with an excellent crystalline quality, smooth surfaces, and a width-to-height aspect ratio > 10^3 such that electron scattering at domain boundaries is negligible. The measured *in situ* and *ex situ* resistivity at 295 K and 77 K as a function of thickness is well-described by the classical Fuchs-Sondheimer (FS) model[26,27] and indicates a lower-bound room-temperature effective mean free path λ_{eff} = 7.4 ± 1.2 nm for Ir layers grown on MgO(001) at 1000 °C. The corresponding $\rho_o\lambda_{eff}$ = (3.8 ± 0.6) ×10^{-16} Ω-m^2 agrees very well with predictions from first principles. However, it is two times larger for T_s = 700 °C, and 26% smaller for annealed layers deposited at T_s = 700 °C, suggesting that $\rho_o\lambda_{eff}$ is strongly affected by atomic-level surface irregularities and/or misfit dislocations even for epitaxial layers. Ir growth on Al_2O_3(0001) leads to a two-domain epitaxial microstructure and an increased resistivity which indicates a 52% probability for electron scattering at grain boundaries described by a 60° rotation about the <111> axis. Overall, the low measured $\rho_o\lambda_{eff}$ product for Ir is smaller than previously reported $\rho_o\lambda$ values of other elemental metals,[8,37,42,44–47] confirming that Ir is a promising alternate interconnect metal for narrow-high conductivity interconnect lines.

II. PROCEDURE

Iridium layers were grown in a three-chamber ultrahigh vacuum DC magnetron sputter deposition system with a base pressure of 10^{-9} Torr.[48] Polished MgO(001) and Al_2O_3(0001) substrates were cleaned by successive ultrasonic baths in trichloroethylene, acetone, isopropanol,

and deionized water. They are then blown dry with nitrogen and mounted onto a Mo holder using colloidal silver paint, introduced into the sputter deposition system via a load lock, and degassed at 1000 °C for 1 hour. Deposition was performed in 10 mTorr 99.999% pure Ar at a constant power of 75 W applied to a 5-cm-diameter 99.9% pure Ir target facing the substrate at a 9 cm distance and with a 45° tilt, yielding a deposition rate of 0.19 ± 0.01 nm/s. The deposition time was adjusted to obtain a series of Ir layers with thickness d = 5–140 nm. A set of four sample series were prepared: Ir deposited (i) on MgO(001) at T_s = 700 °C, (ii) on MgO(001) at T_s = 1000 °C, (iii) on MgO(001) at T_s = 700 °C, immediately followed by *in situ* vacuum annealing at 800, 900, and 1000 °C for 30 min each, and (iv) on Al_2O_3(0001) at T_s = 700 °C followed by the same annealing as for (iii). After deposition, the samples were allowed to cool to room temperature in vacuum for 12 hours, followed by transfer to the analysis chamber for *in situ* resistivity measurements using a 1-100 mA current applied to the outer probes of a linear four-point probe with spring loaded tips and a 1.0 mm inter-probe spacing. Samples were removed from the deposition chamber via a load lock vented to atmospheric pressure using dry N_2 and were immersed in liquid N_2 within 2 s to limit air exposure and possible Ir surface oxidation prior to low-temperature transport measurements. Resistivity measurements at 77 K were taken with a similar linear four-point probe with both sample and probe tips completely immersed in liquid N_2. Subsequent *ex situ* measurements were performed in air with the same setup after the samples were warmed to room temperature by blowing dry N_2 onto the sample to minimize condensed ice/water accumulation on the Ir surface.

X-ray diffraction (XRD) analyses were performed using a PANalytical X'pert PRO MPD system with a Cu source with a parabolic mirror yielding a parallel beam with a <0.055° divergence and a PIXcel solid-state line detector operating in receiving mode with a 0.165 mm active length corresponding to a 2θ opening < 0.04°. Rocking curves were acquired by scanning in ω while keeping the 2θ value fixed to detect the desired 002 or 111 reflections. ϕ scans were acquired using a fixed 2θ value corresponding to Ir 113 reflections and using an offset in ω of 25.24° and 29.50° for 001 and 111 oriented grains, respectively. X-ray reflectivity (XRR) measurements were performed in the same system with the same incident and diffracted beam optics as described above. The measured XRR data were fitted using the PANalytical X'Pert Reflectivity software which employs the Parratt formalism. For this purpose, the densities for Ir, MgO, and Al_2O_3 were kept fixed at 22.4, 3.58, and 3.98 g/cm^3, while the free fitting parameters were the Ir layer thickness, the root-mean-squared (rms) surface roughness, and the rms layer-substrate interface roughness.

Crystallographic orientation maps and pole figures were obtained using electron backscatter diffraction (EBSD) in a VERSA scanning electron microscope (SEM) column with a NordlysNano detector from Oxford Instruments at a pressure of 10^{-6} torr. Secondary electron micrographs and backscatter patterns were obtained with a 10 keV and 1 nA electron beam at a 13 mm working distance. The collected patterns were acquired and analyzed using the Flamenco acquisition software and the HKL Channel 5 software packages from Oxford Instruments, respectively.

III. RESULTS

A. Microstructural Analysis

Figure 1 shows typical x-ray diffraction results from three representative samples. The scans in Fig. 1(a) are from a 100.6 nm-thick Ir layer deposited on MgO(001) substrates at T_s = 1000 °C. The θ-2θ pattern shows a double peak feature due to $CuK_{\alpha1}$ and $CuK_{\alpha2}$ reflections from

the substrate MgO 002 planes and a peak at $2\theta = 47.22°$ which is attributed to Ir 002. This is the only detectable peak from the Ir layer over the entire measured $2\theta = 10\text{-}90°$, indicating a 001 out of plane orientation. The discontinuity of the pattern at $2\theta = 41.32°$ is an experimental artifact due to electronic noise in the line detector caused by the strong reflection from the substrate. The inset shows an ω-rocking curve of the Ir 002 peak from the same sample, indicating a full-width at half-maximum (FWHM) of $\Gamma_\omega^{002} = 0.37°$ which confirms the strong out-of-plane alignment. The plotted ϕ-scan from asymmetric Ir 113 reflections is obtained from the same sample with a constant ω-offset of 25.24° and shows four peaks at 45°, 135°, 225°, and 315°. This observed four-fold in-plane rotational symmetry indicates in-plane alignment of Ir[100] with MgO[100] and, together with the results from the θ-2θ scans, demonstrates a cube-on-cube epitaxial relationship with Ir(001) || MgO(001) and Ir[100] || MgO[100], consistent with the previously reported epitaxial Ir(001)/MgO(001) growth.[49]

Fig. 1(b) shows the XRD results from a 9.9-nm-thick Ir layer deposited at 700 °C and stepwise annealed to 1000 °C. The θ-2θ pattern shows the substrate double-peak feature at $2\theta = 42.92°$ and 43.03°, a strong Ir 111 reflection at $2\theta = 40.60°$ and a much weaker Ir 002 peak at $2\theta = 47.51°$. Laue oscillations indicate smooth interfaces and an Ir thickness of 10.4 ± 0.3 nm, which is in reasonable agreement with $d = 9.9$ nm determined from XRR analyses. The ω-rocking curve of the 111 reflection has a narrow $\Gamma_\omega^{111} = 0.04°$ suggesting excellent crystalline quality. A ϕ-scan from the asymmetric Ir 113 reflection from the same sample is also obtained with a constant ω-offset of 29.50°. It shows twelve peaks, indicating four domains with Ir[10$\bar{1}$], Ir[1$\bar{2}$1], Ir[$\bar{1}$01], or Ir[$\bar{1}$2$\bar{1}$] || MgO[100], with all four domains having the same out-of-plane Ir[111] || MgO[001] direction. These results suggest that this annealed layer contains four-distinct 90°-rotated epitaxial Ir 111 domains which exhibit a good crystalline quality and a strong out-of-plane alignment, and a small fraction of 001 oriented grains.

Fig. 1(c) shows x-ray diffraction results from a 46.7 nm thick Ir layer deposited on Al_2O_3(0001) at T_s = 700 °C followed by *in situ* stepwise annealing to 1000 °C. The θ-2θ pattern shows the substrate double-peak feature at $2\theta = 41.68$ and 41.79° and Ir 111 and Ir 222 peaks at $2\theta = 40.64$ and 87.82°. No other Ir reflections can be detected over the entire measured $2\theta = 10\text{-}90°$, indicating a complete 111 out-of-plane orientation. The well-developed Laue oscillations indicate smooth interfaces and an Ir thickness of 46.2 ± 0.4 nm, in good agreement with $d = 46.7$ nm from XRR analyses. The ω-rocking curve from the 111 reflection has a FWHM $\Gamma_\omega^{111} = 0.46°$. This width is determined by excluding the very sharp peak with $\Gamma_\omega^{111} = 0.03°$ that appears on top of the broader curve and suggests that a portion of the Ir(111) layer forms fully-strained, well-aligned, low-defect-density crystallites which are facilitated by the good in-plane lattice match (1.1% mismatch) between the Ir atoms in the Ir(111) plane and the oxygen atoms in the Al_2O_3(0001) plane. The Ir 113 ϕ-scan from the same sample exhibits six-peaks separated by 60°, indicating two Ir 111-oriented domains that are 60° rotated with respect to each other, where Ir(111) || Al_2O_3(0001) and either Ir[$\bar{1}$01] or Ir[01$\bar{1}$] || Al_2O_3[1$\bar{1}$00].

Figure 2 shows representative x-ray reflectivity curves for Ir layers with $d = 25.4$ and 23.3 nm deposited on MgO(001) and Al_2O_3(0001) substrates, respectively. The measured intensity is plotted as solid red and green lines in a logarithmic scale as a function of the scattering angle $2\theta = 0.2\text{-}4.0°$. The dotted curves are the result from curve fitting using the Parratt formalism for reflectivity and are shifted by a factor of four for clarity purposes. The data fitting describes well the measured characteristic Kiessig fringes and provides values for the film thickness, density, and rms surface and interface roughness. The determined thicknesses $d = 25.4$ and 23.3 nm are in good

agreement (<4% deviation) with 26.6 and 22.9 nm from deposition rate calibrations. The measured surface roughness σ = 0.33 and 0.32 nm indicates smooth Ir surfaces on both MgO(001) and Al_2O_3(0001) substrates. Similarly, the roughness values of the layer-substrate interfaces are 0.63 and 0.27 nm, suggesting negligible chemical reaction at the interface. We note that adjusting the fitting procedure by adding a 0.2-nm-thick Ir-oxide surface layer to the model decreases the fit quality (increases χ^2), suggesting that our Ir layers have a negligible (< 0.2 nm) surface oxide. The thickness and roughness data from XRR analyses of all Ir layers in this study are summarized in Tables 1 and 2, and briefly discussed below. We note that the layer thickness for the thickest sample with d = 133.1 nm is determined from the deposition rate and time, since the spacing between XRR fringes is too small to be resolved for this sample.

XRD and XRR analyses are performed for all 22 samples from the four series in this study, yielding the following overall results:

(1) Ir deposited on MgO(001) at T_s = 1000 °C yields epitaxial single-crystal Ir(001) layers with an increasing crystalline quality with increasing thickness, as evidenced by the Ir 002 ω rocking curve width which decreases from Γ_ω^{002} = 1.3 to 0.37° for d = 7.7 – 100.6 nm. The RMS roughness measured from XRR is small ($\sigma \leq$ 0.53 nm) for thick ($d \geq$ 19.5 nm) layers but becomes larger (σ = 0.87-1.1 nm) at small thickness d = 7.7-11.5 nm (as also summarized in Table 1). This increase is attributed to a discontinuous microstructure for $d \leq$ 11.5 nm. More specifically, the layer with d = 7.7 nm consists of separated islands with negligible coalescence as determined from SEM micrographs as the one shown as Supplementary Figure S1. Increasing d to 11.5 nm results in considerable but incomplete coalescence as indicated by the micrograph shown as Supplementary Figure S2, showing partial surface coverage with elongated islands. This discontinuous microstructure for d < 19.5 nm is attributed to the thermodynamic driving force for dewetting, caused by the surface energy which is expected to be larger for the metallic Ir layer than the ceramic MgO substrate. The discontinuous microstructure causes a large sheet resistance and motivates growth at lower temperatures as done in the following sample series.

(2) Ir deposited on MgO(001) at T_s = 700 °C also yields epitaxial single-crystal Ir(001) layers. A representative set of XRD scans is provided as supplementary Figure S3. The Ir 002 ω rocking curve width ranges from Γ_ω^{002} = 1.9 to 0.67° for d = 6.8 – 133.1 nm, indicating a lower crystalline quality than for T_s = 1000 °C. The surface roughness $\sigma \leq$ 0.46 nm is smaller for T_s = 700 °C than for T_s = 1000 °C for all d. Thus, reducing T_s from 1000 °C to 700 °C is effective in limiting the adatom mobility to suppress dewetting and the formation of a discontinuous microstructure at small d. However, the limited atomic diffusion also results in a lower crystalline quality.

(3) Ir deposition on MgO(001) at T_s = 700 °C with subsequent step-wise vacuum annealing to 1000 °C results in a microstructure which is strongly affected by the layer thickness. Thick layers with d = 46.4 - 103.9 nm are epitaxial Ir(001) single crystals with a good crystalline quality (Γ_ω^{002}= 0.6°- 0.8°) and small rms surface roughness ($\sigma \leq$ 0.39 nm). *In situ* annealing causes a small/negligible 3-9% reduction in Γ_ω^{002} and a negligible improvement in the surface smoothness in comparison to the as-deposited layers with T_s = 700 °C, suggesting no effect from annealing for layers with $d \geq$ 46.4 nm. However, as discussed below, annealing causes an overall reduction in the resistivity which we attribute to some improvement in crystalline quality or surface smoothness that is not detected by our XRD and XRR analyses. In contrast to these thick layers, annealed layers with d = 5.2, 9.9 and 19.5 nm exhibit a multi-domain microstructure with primarily 111-oriented and some residual 001-oriented domains, with a measured XRD 111-vs-002 peak

intensity ratio I_{111}/I_{002} = 15, 117, and 4, respectively. That is, while the as-deposited layers exhibit a pure 001 orientation as discussed above, subsequent annealing causes a transition to microstructures with 111-oriented grains. We attribute this to renucleation of 111-oriented grains during the annealing procedure. The driving force for this transition is not known but may be related to strain relaxation or a reduction in the surface energy which is lower for Ir(111) than Ir(001).[50] The transition is most prominent for thin ($d \leq 9.9$ nm) layers, is less dominant for d = 19.5 nm as indicated by the smaller I_{111}/I_{002}, and is completely suppressed for $d \geq 46.4$ nm. The measured rocking curve widths of the 111-oriented grains, Γ_ω^{111} = 0.054°, 0.049°, and 0.031° for d = 5.2, 9.9 and 19.5 nm, respectively, are approximately an order of magnitude smaller than the as-deposited Γ_ω^{002}, indicating an excellent crystalline quality of the renucleated grains. Γ_ω^{111} decreases with decreasing d, suggesting wider renucleated domains for the thinner layers, consistent with the EBSD data presented below. In addition, the measured σ = 0.23, 0.16, and 0.39 nm indicate that the surface roughness during annealing (including renucleation) decreases by 36-65%.

(4) All layers deposited on Al_2O_3(0001) at T_s = 700 °C and followed by *in situ* stepwise annealing to 1000 °C are 111-oriented two-domain epitaxial layers with Γ_ω^{111} decreasing from 1.9° - 0.36° for d = 6.4 – 89.3 nm. The surface roughness is small, $\sigma \leq 0.46$ nm, for all layers. Their microstructure consists of two epitaxial domains which are related to each other by a 60° or 180° rotation about the [111] axis along the growth direction. We attempt to estimate the average separation between domain boundaries from the in-plane coherence length determined from the ω-rocking curve width.[51] This analysis is convoluted because the rocking curves consist of a broad and narrow peak from strained and relaxed sections of the layer. The broad peak widths yield an in-plane coherence length that increases from D_{broad} = 6.5 to 15.5, 19.3, 27.0, and 35.3 nm for d = 6.4, 12.6, 23.3, 46.7, and 89.3 nm, while the coherence lengths from narrow peaks indicate an approximately thickness-independent D_{narrow} = 300 – 400 nm. The large variation in the domain sizes based on the XRD analyses, from 6.5 – 400 nm for these Ir(111)/Al_2O_3(0001) layers, may be an artifact caused by a non-uniform development of misfit dislocations and related strain relaxation. Correspondingly, alternate measurements to determine the domain size are used, as described in the following.

Figure 3 shows secondary electron SEM micrographs, EBSD inverse pole figure (IPF-X) orientation maps and {100} pole figures from four representative Ir layers. The micrograph in Fig. 3(a) is from a 100.6-nm-thick epitaxial Ir(001)/MgO(001) layer grown at T_s = 1000 °C. The micrograph exhibits negligible contrast variations, indicating a continuous layer with a relatively smooth surface and no pits. This is consistent with the small surface roughness σ = 0.53 nm measured by XRR. We note that pits due to dewetting would result in evident contrast, similar to what is detected for thin layers that are annealed [supplementary Fig. S4]. The IPF-X orientation map in Fig. 3(a) is from the same sample area as the secondary electron micrograph. It is completely red, indicating a single [100] in-plane orientation. That is, Ir[100] is aligned with the horizontal x-axis which also corresponds to the MgO[100] direction, confirming the single-crystal Ir(001)/MgO(001) cube-on-cube epitaxial relationship detected by the XRD results presented in Fig. 1(a). This is also consistent with the Ir{100} pole figure in Fig. 3(a), showing a central peak indicating the 001-growth direction and a single-set of four-fold symmetric peaks at an angle of 90°, confirming a single in-plane orientation.

Fig. 3(b) shows results from a 46.7-nm-thick Ir(111) layer grown on Al_2O_3(0001). The secondary electron micrograph exhibits negligible contrast, consistent with a smooth surface, with σ = 0.28 nm measured by XRR. The Ir{100} pole figure shows 6-fold symmetric peaks at an angle of 54°, indicating a single 111 out-of-plane direction with two domains which are rotated by 60°

with respect to each other. The two domains appear in nearly identical shades of green in the IPF-X map, indicating that both exhibit an Ir<$\bar{1}$01> type in-plane orientation along the horizontal direction of the micrograph which corresponds to the in-plane $Al_2O_3[1\bar{1}00]$ substrate direction. Thus, this analysis confirms the layer-substrate epitaxial relationship determined from XRD, with the two Ir domains having their in-plane Ir[$\bar{1}$01] or Ir[01$\bar{1}$] direction || $Al_2O_3[1\bar{1}00]$. A quantitative analysis of the IPF-X orientation map yields an average lateral domain size D_{avg} = 88 nm, which is within the range estimated from the XRD rocking curves discussed above.

Fig. 3(c) shows orientation data from a 9.9-nm-thick Ir layer deposited on MgO(001) at 700 °C and stepwise annealed to 1000 °C. The secondary electron micrograph shows contrast variations which suggest a polycrystalline microstructure with 20-70 μm wide grains. The corresponding IPF-X map from the same sample area confirms that these apparent grains are, in fact, domains with distinct in-plane orientations. The corresponding {100} pole figure exhibits 12 peaks, indicating four 111-oriented domains which are 90° rotated with respect to each other about the 111 growth direction. Thus, the orientation map shows four Ir domains colored in purple, violet, green, and green, which have their [$\bar{1}2\bar{1}$], [1$\bar{2}$1], [10$\bar{1}$], and [$\bar{1}$01], directions parallel to MgO[100], respectively, suggesting local epitaxy of each domain. We note that the domains are very large, their width of 20-70 μm is over three orders of magnitude larger than their height, which corresponds to the layer thickness of 9.9 nm. Thus, we hypothesize that the domains form in a nucleation-limited growth during annealing of the as-deposited epitaxial Ir(001) layer. Nucleation may occur at defect sites at the layer-substrate interface, followed by subsequent lateral near diffusion-less growth. The driving force for this renucleation is likely a combination of the surface energy which is lower for the close-packed Ir(111) vs the Ir(001) surface as well as the out-annealing of dislocations and associated strain fields caused by the misfit of epitaxial as-deposited Ir(001) on MgO(001). The pole figure plotted in Fig. 3(c) has no detectable central peak, indicating that the density of residual 001-oriented domains is negligible and that renucleation during annealing results in a nearly complete transition from 001 to 111-oriented domains, consistent with the 117 times stronger 111 vs 002 peak in the θ-2θ pattern from the same sample in Fig. 1(b). In contrast, the polefigure in Fig. 3(d) from an annealed layer with d = 19.5 nm exhibits both, 12 peaks at a 54° angle as well as a central peak and four peaks at 90°, indicating a mixture of the domains discussed in Figs. 3(a) and (c). More specifically, a fraction of this layer consists of four 111-oriented domains that appear in purple, violet, green and green in the IPF-X map, but also residual 001-oriented Ir which appears in red and has not transformed during annealing. The micrograph in Fig. 3(d) is purposely recorded from an area of the sample with approximately equal fractions of renucleated and residual domains to illustrate the mixed domain microstructure. However, a larger area analysis shown in Supplementary Fig. S5 suggests that this layer is predominantly 001 oriented with a small fraction of renucleated 111 domains. We note that the XRD θ-2θ pattern from this sample (not shown) has a 111 vs 002 peak intensity ratio of 4, which is primarily attributed to the much stronger crystalline alignment or the renucleated 111 domains. The factor of 4 is much smaller than 117 mentioned above for the 9.9-nm-thick layer, confirming the observed trend of a considerably smaller fraction of grain renucleation for the thicker layer.

We note that reducing the thickness further to below ~10 nm results in a discontinuous microstructure with a partial coverage of the substate by the deposited Ir, as determined by electron microscopy analyses. An example micrograph from a d = 5.2 nm layer deposited at T_s = 700 °C followed by *in situ* annealing is provided as Supplementary Figure S4. It shows 40-200 nm wide holes in the layer which extend to the substrate and are terminated by six facets along Ir <110>, indicating dewetting for this d = 5.2 nm layer during deposition at 700 °C and/or annealing at 1000

°C, similar to what has been reported for single-crystal Ni(001) layers grown on MgO(001) at room temperature and annealed to 900 °C.[52] We attribute the dewetting to the larger surface energy of the metallic Ir layer than the ceramic MgO substrate. An out-of-plane orientation map from the same d = 5.2 nm sample indicates strong 111 preferred orientation with no evidence of residual 001-domains, in agreement with XRD θ-2θ scans. The corresponding {100} pole figure exhibits 6 poles indicating two epitaxial domains in contrast to 4 domains observed for d = 19.5 and 9.9 nm layers, suggesting possibly an even faster lateral grain growth for the thinner layer, consistent with the narrowest rocking curve width for this d = 5.2 nm layer.

In summary, the EBSD analyses confirm the XRD results, showing that layers deposited on MgO(001) at 1000 °C are epitaxial single-crystal Ir(001) while layers grown on Al_2O_3(0001) form 111-oriented two-domain microstructures with an average domain width D = 88 nm. Most interesting are the layers deposited on MgO(001) at 700 °C and annealed to 1000 °C: The as-deposited layers are epitaxial Ir(001). Annealing causes renucleation of 111-oriented grains for $d \leq$ 19.5 nm. The 111-oriented grains are very wide, with aspect ratios exceeding three orders of magnitude, and form four domains with a local epitaxy with the substrate. Annealing causes complete transformation to a 111-oriented layer for d = 5.2 and 9.9 nm, but only partial renucleation for the d = 19.5 nm layer which exhibits a large fraction of residual Ir(001) domains, and no renuclation for $d \geq$ 46.4 nm, suggesting a clear thickness effect. To explore this further, an additional layer was deposited with a measured d = 10.0 nm, which is identical (within experimental uncertainty) to the d = 9.9 nm layer. Its EBSD analysis (see Supplementary Figure S6) indicates a significantly higher fraction of residual 001-oriented domains as well as a higher fraction of random grain boundaries than the 9.9 nm thick Ir layer discussed previously. In fact, this new d = 10.0 nm exhibits a microstructure comparable to the d = 19.5 nm layer presented in Fig. 3(d). This result suggests a considerable stochasticity in the renucleation process. From the overall data, we derive an approximate critical thickness 5 nm < $d_c \leq$ 10 nm for complete transformation while partial transformation occurs between d = 10 and 40 nm. The large domain sizes particularly for completely transformed layers minimizes electron scattering at grain (domain) boundaries, as discussed in Section IV.

B. Electron Transport

Figure 4 shows the resistivity ρ measured *in situ* at 295 K and at liquid nitrogen at 77 K vs thickness d from the four series of Ir layers presented above. The data is also summarized in Tables 1 and 2. The plotted ρ increases with decreasing d for all four series and at both temperatures. This is attributed to electron scattering at the Ir top and bottom surfaces. The plotted blue triangles are data from the samples deposited at T_s = 1000 °C. The thickest layer (d = 100.6 nm) in this series has a room-temperature resistivity ρ = 5.37 ± 0.26 μΩcm. This is identical (within experimental uncertainty) to the reported Ir bulk resistivity ρ_o = 5.2 μΩcm,[53] indicating a negligible resistivity size effect for d = 100.6 nm at 295 K. The resistivity increases to ρ = 5.44 ± 0.02 and 6.04 ± 0.04 μΩcm with decreasing thickness d = 46.0 and 19.5 nm. Decreasing the thickness further to d = 11.5 nm leads to a dramatic 248% resistivity increase to ρ = 18.7 ± 0.2 μΩcm which is outside the plotted range, while the resistivity of the layer with d = 7.7 nm could not even be measured with our experimental setup, indicating $\rho > 10^6$ μΩcm and suggesting that the 7.7-nm-thick sample is discontinuous. This is consistent with the dewetting arguments presented above and the relatively large measured surface roughness σ = 1.1 and 0.87 nm for the nominally 7.7 and 11.5 nm thick layers, respectively, suggesting that the thin film nuclei have not coalesced for d = 7.7 nm and that coalescence occurs approximately at d = 11.5 nm, resulting in a partially discontinuous layer and

a correspondingly high ρ for the 11.5 nm thick layer. We note that the latter layer has a measured σ = 0.87 nm which is twice the roughness of the d = 19.5 and 46.0 nm layers, such that the large ρ can partially be attributed to a roughness effect.[17,54]

The purple diamonds in Fig. 4 indicate the measured resistivity of six layers deposited at a lower T_s = 700 °C. The resistivity could be measured for all thicknesses d = 6.8-133.1 nm and the surface roughness is relatively low (σ < 0.46 nm) for all samples in this series, indicating that the lower T_s results in continuous layers which is attributed to the reduced adatom mobility at lower temperatures. The room-temperature resistivity of the thickest layer with d = 133.1 nm is 14% larger than the reported Ir bulk resistivity,[53] indicating considerable electron scattering at crystalline defects. In fact, all layers deposited at T_s = 700 °C are significantly (13-27%) more resistive than continuous layers with a comparable d but deposited at T_s = 1000 °C. Thus, the reduction from 1000 to 700 °C results in a degradation of the crystalline quality, which is in perfect agreement with the measured 64-81% increase in the measured ω rocking curve width.

The red circles in Fig. 4 show the resistivity from Ir layers deposited at T_s = 700 °C followed by *in situ* step-wise annealing to 800, 900, and 1000 °C for 30 min each. This deposition and annealing procedure is chosen in an attempt to simultaneously obtain the high crystalline quality characteristic for T_s = 1000 °C with the continuous layer microstructure at small d observed for T_s = 700 °C. However, as discussed above, annealing causes a transformation into a multi-domain polycrystalline microstructure containing renucleated 111-domains for $d \leq$ 19.5 nm. The resistivity ρ = 6.41 ± 0.31 μΩcm of the d = 9.9 nm layer is particularly low. It is 34% below the as-deposited layer (purple diamond) and just 23% above the Ir bulk resistivity. In comparison, the resistivity for 10-nm-thick epitaxial Cu(001),[8] Co(0001),[37] W(110),[45] Mo(110),[38] Rh(001),[44] and Ru(0001)[42] layers is 168%, 89%, 86%, 64%, 54%, and 30% larger than their bulk resistivity, respectively. That is, the resistivity size effect for this Ir layer is considerably smaller than for other known metals. We attribute the resistivity reduction during annealing to a considerable increase in the crystalline quality and surface smoothness during the renucleation process. The XRD, XRR and EBSD analyses discussed above indicate a reduction in the rocking curve width by 1-2 orders of magnitude, a 3-fold reduction in the surface roughness to σ = 0.16 nm, and a domain size of 10-200 μm. The latter value is 10^3 times larger than the predicted electron mean free path such that electron scattering at grain (domain) boundaries has a negligible effect on the resistivity. The annealed layer with a two times larger thickness d = 19.5 nm has a ρ = 6.55 ± 0.12 μΩcm that is slightly larger (equal within experimental uncertainty) than for d = 9.9 nm. This is opposite to the trend of an increasing ρ with decreasing d and is attributed to the incomplete transformation (presented above) which results in residual 001 oriented domains that have a lower crystalline quality and a 2.4 times higher surface roughness than the renucleated 111-oriented domains. We note that ρ for this layer is 8% larger than for the epitaxial Ir(001) layer with a similar d but deposited at T_s = 1000 °C (blue triangle). This difference is attributed to a 25% larger Γ_ω^{002} = 1.12° for the annealed layer in comparison to Γ_ω^{002} = 0.90° for the layer deposited at T_s = 1000 °C, suggesting a higher density of crystalline defects for this annealed layer and consequently a higher resistivity due to additional electron scattering at these defects. The thinnest annealed layer with d = 5.2 nm has a considerably larger ρ = 11.3 ± 0.5 μΩcm which we attribute to the non-uniform surface coverage caused by dewetting during annealing as discussed above and shown in Fig. S4.

The resistivity of the fourth series of Ir layers deposited on Al_2O_3(0001) substrates is plotted in Fig. 4 as green square symbols. The measured values are also tabulated in Table 2. Like

for the other Series, ρ increases with decreasing d which is attributed to electron scattering at surfaces. However, the resistivity is larger than for the Ir deposited on MgO(001) at 1000 °C or at 700 °C and annealed to 1000 °C. This is attributed to additional electron scattering at the 60° in-plane rotated domain boundaries for the Ir(111)/ Al_2O_3(0001) layers, as discussed quantitatively in Section IV.

Tables 1 and 2 include *ex situ* room-temperature resistivity values. They are measured after sample removal from the deposition system and low temperature measurements, as described in Section II. The values are slightly larger than the *in situ* ρ measured before air exposure. However, the increase is smaller than the experimental uncertainty for most samples and < 6% for all Ir layers in this study. This suggests that Ir surface oxidation causes a slight or negligible decrease in surface scattering specularity as discussed in Section IV.

Figure 4 includes the resistivity measured at 77 K from the four Series of Ir layers. They are plotted as open symbols and are also included in Tables 1 and 2. The values are lower than for 295 K, due to the reduced electron-phonon scattering at 77 K, but the increase in ρ with decreasing d is nearly independent of temperature. Thus, the resistivity difference $\Delta\rho$ between the two temperatures is nearly thickness independent. More specifically, $\Delta\rho$ = 4.40, 4.31, and 4.41 μΩcm for Ir/MgO(001) with d = 100.6, 46.0, and 19.5 nm and T_s = 1000 °C, and $\Delta\rho$ = 4.56, 4.56, 4.68, 4.71, 5.03, and 3.4 μΩcm for d = 131.1, 66.1, 25.4, 13.7, 9.6, and 6.8 nm and T_s = 700 °C. For the annealed layers, $\Delta\rho$ = 4.37, 4.16, 4.64, 5.03, 4.54, and 6.4 μΩcm for d = 103.9, 46.4, 19.5, 10.0, 9.9, and 5.2 nm, and for Ir(111)/Al_2O_3(0001) $\Delta\rho$ = 4.19, 4.39, 4.44, 4.43, and 4.86 μΩcm for d = 89.3, 46.7, 23.3, 12.6, and 6.4 nm. These values are in good agreement with the reported $\Delta\rho$ = 4.54 μΩcm for bulk Ir, suggesting that the resistivity contributions from electron scattering at surfaces, grain boundaries, and phonons are nearly additive and follow Matthiessen's rule.

IV. DISCUSSION

We now discuss the measured resistivity size effect in epitaxial Ir layers using the semiclassical transport models by Fuchs and Sondheimer (FS) for surface scattering[26,27] and Mayadas and Shatzkes (MS) for grain boundary scattering.[28] The FS model describes resistivity scaling due to electron scattering at the surfaces by two parameters: (1) the electron phonon scattering mean free path λ and (2) the surface scattering specularity p which can be further divided into p_1 and p_2 for the top Ir surface and bottom Ir/substrate interface.[12] Measured ρ vs d data typically cannot uniquely determine both p and λ.[8] To circumvent this problem, we set $p_1 = p_2 = 0$ (assuming electron surface scattering is completely diffuse) and obtain a lower bound to the effective mean free path λ_{eff} by fitting a FS curve to the measured resistivity using the exact version of the FS model.[12,42] Thus, in the following, the presented λ values should be interpreted either as (a) a lower limit of possible λ values, or (b) the λ under the assumption of completely diffuse surface scattering. We note that our data analysis is complicated by the fact that epitaxial Ir layers in our study exhibit (a) film discontinuity for d < 19.5 (T_s = 1000 °C), (b) poor crystalline quality (T_s = 700 °C), or (c) a multi-domain microstructure (T_s = 700 °C followed by *in situ* stepwise annealing) on MgO(001) and Al_2O_3(0001) substrates.

We begin our analysis by fitting the FS model to resistivity data from Ir(001) oriented layers grown at T_s = 700 °C, because these are epitaxial single crystal layers with no grain boundaries and negligible dewetting. The solid and dashed purple lines in Figure 4 are the result from such curve fitting to the resistivity measured at 295 and 77 K, respectively, using as fitting

parameters the bulk resistivity ρ_o and the effective electron mean free path λ_{eff}. This yields ρ_o = 5.75 ± 0.09 μΩcm and λ_{eff} = 14.3 ± 0.8 nm at 295 K, and ρ_o = 1.07 ± 0.12 μΩcm and λ_{eff} = 83 ± 16 nm at 77 K, as also listed in Table 3. These values indicate that reducing the temperature from 295 to 77 K lowers ρ_o five-fold but increases λ six-fold, resulting in an approximately temperature-independent product $\rho_o\lambda_{eff}$ = (8.2 ± 0.4) × 10^{-16} and (8.9 ± 1.8) × 10^{-16} Ωm^2 at 295 K and 77 K, respectively. The decrease in ρ_o and increase in λ_{eff} are a direct consequence of the reduced electron-phonon scattering and the temperature-independence of $\rho_o\lambda_{eff}$ is expected from classical electron transport models with a negligible temperature-dependence in the electronic structure.[39] We note that the ρ_o values are 11% and 62% above the reported bulk resistivity at 295 and 77 K, respectively. This is attributed to electron scattering at crystalline defects which causes an increase in ρ_o. The defects may include threading dislocations, stacking faults, vacancies, strain-fields near the layer-substrate interface and edge dislocations which account for crystalline misalignment. The defects are due to the limited adatom mobility at T_s = 700 °C which, as previously discussed, leads to a limited crystalline quality with a relatively large XRD rocking-curve width Γ_ω^{002} = 0.67 – 1.9°. The measured Γ_ω^{002} decreases with increasing thickness such that the defect density is likely also a function of d and, in turn, the "bulk resistivity" is no longer independent of d for this sample series, as is assumed during the fitting procedure. Consequently, the $\rho_o\lambda_{eff}$ value deduced for this series may not represent an intrinsic property of Ir because it could be strongly affected by the thickness-dependence in the defect concentration. We note that we do not consider grain boundary scattering in this analysis because a small-angle boundary with a ~1° tilt (corresponding to the rocking curve width) corresponds to an array of edge dislocations which are vertically separated by 16 nm, assuming the Burgers vector equals the interatomic spacing of 0.27 nm. Thus, "grain boundaries" for d = 10-50 nm would consist of zero to three dislocations which are more appropriately described as discrete crystalline line defects rather than as a 2D grain boundary.

We apply a similar fitting procedure for Ir layers grown at 1000 °C, yielding the solid and dashed blue lines in Figure 4. The layers with d = 11.5 and 7.7 nm are not considered for this data analysis due to their discontinuous microstructure and resulting large resistivity. Data fitting yields a room temperature ρ_o = 5.17 ± 0.08 μΩcm which matches the reported Ir bulk resistivity of 5.2 μΩcm, suggesting negligible defect scattering which renders the deduced data more reliable than for T_s = 700 °C. In contrast, a minor effect from defect scattering can be detected from analysis of the low-temperature data yielding ρ_o = 0.80 ± 0.04 μΩcm which is 21% above the reported 0.66 μΩcm for bulk Ir at 77 K.[53] The fitting indicates a room-temperature λ_{eff} = 7.4 ± 1.2 nm and a corresponding temperature-independent $\rho_o\lambda_{eff}$ = (3.8 ± 0.6) ×10^{-16} and (3.5 ± 0.4) ×10^{-16} Ωm^2 for 295 and 77 K, respectively. These values are quite small, indicating a small resistivity scaling for Ir. More specifically, $\rho_o\lambda_{eff}$ = 3.8 ×10^{-16} Ωm^2 is 1.7, 2.6, 3.2, 1.3 and 1.2 times smaller than the reported values for competing interconnect materials like Cu with 6.7×10^{-16} Ωm^2,[8] W with 10.1×10^{-16} Ωm^2,[45] Co with 12.2×10^{-16} Ωm^2,[37] Ru with 5.06×10^{-16} Ωm^2,[42] and Rh with 4.5×10^{-16} Ωm^2,[44] respectively. That is, $\rho_o\lambda_{eff}$ for Ir is smaller than that of all previously measured elemental metals, indicating great promise for Ir as an alternative metal for narrow high-conductivity interconnects. The impact of this small $\rho_o\lambda_{eff}$ on the resistance of polycrystalline interconnect lines has been estimated in Refs. 38 and 41, suggesting that Ir will outperform all other elemental metals for narrow lines. The measured $\rho_o\lambda_{eff}$ = 3.8 ×10^{-16} Ωm^2 for Ir is also in excellent agreement with $\rho_o\lambda$ = 3.69 ×10^{-16} Ωm^2 calculated from first principles.[39]

The red solid and dashed lines in Fig. 4 are from fitting ρ vs d data from the Ir layers deposited at 700 °C and annealed to 1000 °C. The analysis excludes the layer with d = 5.2 nm due

to its non-uniform surface coverage. The resulting mean free paths λ_{eff} = 5.1 ± 1.8 and 11.8 ± 4.8 nm at 295 and 77 K, respectively, and the corresponding $\rho_o\lambda_{eff}$ = (2.8 ± 1.0) ×10^{-16} and (1.5 ± 0.6) ×10^{-16} Ωm^2. We note that the uncertainty in the deduced $\rho_o\lambda_{eff}$ is quite large, as the data is not very well described by the FS curve. We attribute this to a changing microstructure with varying d. More specifically, as discussed above, $d \geq$ 46.4 nm results in an 001-oriented epitaxial microstructure, the layer with d = 19.5 nm exhibits a mixture of residual 001 and renucleated 111-oriented domains, while the two nominally identical layers with d = 9.9 and 10.0 nm show a different degree of transformation: The d = 9.9 nm layer has almost completely transformed into a multi-domain 111-oriented microstructure and has a 10% lower resistivity than the d = 10.0 nm layer with a mixed-domain microstructure similar to that for d = 19.5 nm. This suggests that the renucleation process leads to a reduction in the resistivity which we attribute to the excellent crystalline quality and low surface roughness of renucleated 111-oriented Ir domains, resulting in the lower resistivity for the d = 9.9 nm layer which exhibits a nearly complete transformation. To summarize: the measured ρ is lower for the annealed layers than for the as deposited T_s = 700 °C samples, indicating that annealing improves the crystalline quality and lowers ρ. However, for samples where annealing causes only a limited or no renucleation of the 001-oriented crystal, the measured ρ is larger than for T_s = 1000 °C. This is because growth at 700 °C followed by annealing at 1000 °C leads to lower crystalline perfection than growth at 1000 °C, which is due to the lower activation barrier for surface than bulk diffusion which facilitates more effective mass transport during deposition than post-deposition annealing. In contrast, samples with nearly complete renucleation during annealing exhibit the largest crystalline quality and a corresponding low resistivity, exemplified by the d = 9.9 nm layer. Due to this thickness-dependent crystalline quality, the $\rho_o\lambda$ product deduced from the third series likely underestimates the actual intrinsic value of Ir.

We discuss now the resistivity of Ir(111) layers grown on Al_2O_3(0001) substrates. Ir(111) layers have an increased resistivity which we attribute to additional electron scattering at the domain walls between 60° in-plane rotated domains. The approximate form of the MS model predicts that electron scattering at grain boundaries causes an additive resistivity term $\Delta\rho_{gb} = 3\rho_o\lambda R/[2D(1-R)]$.[12] Thus, $\Delta\rho_{gb}$ is a function of $\rho_o\lambda$, the grain size D and the reflection coefficient R. For our Ir(111)/Al_2O_3(0001) layers, D corresponds to the average lateral domain size D_{avg} = 88 nm, as determined by EBSD. Both XRD and EBSD analyses indicate that the grain boundary type (60° rotation about the <111> axis) is independent of d. We therefore assume R and D and, in turn, also $\Delta\rho_{gb}$ to be independent of the Ir(111) layer thickness. Correspondingly, data fitting for the Ir(111) resistivity is done by adding a constant $\Delta\rho_{gb}$ to the FS model predictions, where $\Delta\rho_{gb}$ is a thickness-independent fitting parameter. We use a fixed ρ_o = 5.17 μΩcm at 295 K and ρ_o = 0.80 μΩcm at 77 K from the layers with T_s = 1000 °C to perform data fitting, yielding the solid and dashed green lines in Fig. 4 and values for $\rho_o\lambda_{eff}$ of (4.5 ± 0.5)×10^{-16} and (4.7 ± 0.4)×10^{-16} Ωm^2 at 295 K and 77 K, respectively, and a $\Delta\rho_{gb}$ = 0.86 ± 0.19 and 0.84 ± 0.12 μΩcm at 295 K and 77 K, respectively. These two $\Delta\rho_{gb}$ values are identical within experimental uncertainty, indicating that grain boundary scattering is temperature-independent, as expected from the approximate MS model. We determine the grain boundary reflection coefficient R from the above expression for $\Delta\rho_{gb}$, using D_{avg} = 88 nm and $\rho_o\lambda$ and $\Delta\rho_{gb}$ from the data fitting, yielding R = 0.52 ± 0.02 and 0.51 ± 0.03 at 295 K and 77 K, respectively. These values are larger than the previously measured R = 0.26,[2] 0.43,[55] or 0.30[12] for Cu but are within the large range of reported first-principles predictions for the reflection coefficient R = 0.02 – 0.56 of high-symmetry grain boundaries (Σ3, Σ5, Σ9, and Σ11) in metals including Ir, Rh, Cu, Pt, Pd, and Co.[16,25,44,56,57] We note that our measured R = 0.52

± 0.02 is for a specific grain boundary which is characterized by a 60° rotation about the <111> axis. Similarly, the high-symmetry coherent Σ3 boundary for which the predicted $R = 0.16$[56] or 0.25[41] can also be defined by a 60° rotation about the <111> axis. However, for the former the grain boundary is parallel and for the latter perpendicular to the <111> rotation axis, such that the large difference in R may be attributed to the boundary orientation even for identical relative grain orientations.

Our results indicate a slight increase in the room-temperature resistivity upon air exposure for all four Ir sample series. This increase can be attributed to experimental uncertainty but may also indicate a decrease in the surface scattering specularity caused by surface oxidation, similar to what has previously been reported for Ni,[47] Nb,[46] Co,[37] and Cu.[8] To quantify this effect, we follow the procedures in Refs. 44,46,47 and attribute the resistivity increase to a decrease in the room-temperature scattering specularity Δp_1 at the top surface of the Ir layers. Data fitting of the measured *ex situ* room temperature resistivity yields $\Delta p_1 = -0.09 \pm 0.03$, -0.14 ± 0.11, -0.46 ± 0.36, and -0.12 ± 0.10 for the four Ir layer series grown on MgO(001) at $T_s = 700$ °C, 1000 °C, $T_s = 700$ °C and annealed, and on Al_2O_3(0001), respectively. The overall average $\Delta p_1 = -0.20 \pm 0.15$ is relatively modest and similar in magnitude to the error bar, confirming that the observed effect can potentially be ascribed to experimental uncertainty. Its magnitude is smaller than the reported $\Delta p_1 = -0.6$ or -0.7 reported for Cu,[8,20] -0.4 for Ag,[13] and -0.9 or -0.8 for Nb,[46] and similar to the negligible air-exposure effect reported for Ru,[42] W,[45] and Rh.[44] The small to negligible effect of oxygen exposure on the electron scattering at Ir surfaces is promising for potential liner-free Ir interconnects which would be in direct contact with an oxidizing dielectric.

V. CONCLUSIONS

Ir growth on MgO(001) at $T_s = 1000$ °C leads to smooth epitaxial Ir(001) layers for $d \geq 19.5$ nm, but to a high roughness and a discontinuous layer if the thickness is reduced to $d = 11.5$ and 7.7 nm, respectively. The continuity problems are resolved with a reduced $T_s = 700$ °C which, however, causes a lower crystalline quality with a 45% smaller in-plane x-ray coherence length. Growth at $T_s = 700$ °C followed by step-wise *in situ* annealing to 1000 °C results in smooth layers with a high crystalline quality but grain re-nucleation and a multi-domain epitaxial microstructure. That is, the Ir microstructure and surface morphology is strongly affected by both deposition conditions and layer thickness, making direct experimental quantification of the resistivity size effect challenging. Fitting the measured ρ vs d at 295 and 77 K to the Fuchs-Sondheimer model indicates a lower-bound room-temperature effective mean free path $\lambda_{eff} = 7.4 \pm 1.2$ nm and a corresponding temperature-independent $\rho_o\lambda_{eff} = (3.8 \pm 0.6) \times 10^{-16}$ Ωm^2. This $\rho_o\lambda_{eff}$ is in good agreement with the $\rho_o\lambda = 3.69 \times 10^{-16}$ Ωm^2 determined from first principles. However, it is 116% larger for as-deposited layers at $T_s = 700$ °C and 26% smaller for annealed layers deposited at $T_s = 700$ °C. We note that the small $\rho_o\lambda_{eff} = (2.8 \pm 1.0) \times 10^{-16}$ Ωm^2 evaluated from the annealed layers has a relatively large uncertainty due to a non-uniform microstructure for the layers in this series: Layers with $d \leq 19.5$ nm exhibit a mixture of residual 001 and renucleated 111 domains, with an increasing renucleated volume fraction as the layer thickness decreases. The renucleated domains exhibit a low surface roughness $\sigma = 0.2$ nm, a low x-ray diffraction rocking-curve width of 0.04°, and are 20-70 μm wide, corresponding to a $>10^3$ width-to-height aspect ratio. The resulting large distance between domain boundaries makes electron scattering at boundaries negligible.

Ir(001)/MgO(001) layers with $d \geq 46.4$ nm and $T_s = 700$ °C do not undergo renucleation during annealing, yielding a lower crystalline quality and higher resistivity in comparison to layers grown directly at 1000 °C. Ir growth on Al_2O_3(0001) substrates yields a two-domain epitaxial microstructure with an average domain size $D = 88$ nm, evaluated from electron backscatter diffraction orientation maps. The domain boundaries are described by a 60° rotation about the <111> axis and cause a thickness independent resistivity contribution $\Delta\rho_{gb} = 0.86 \pm 0.19$ and 0.84 ± 0.12 μΩcm at 295 and 77 K, indicating an electron reflection coefficient $R = 0.52 \pm 0.02$. The overall results suggest that resistivity scaling in Ir is strongly influenced by microstructural features including strain fields from misfit-dislocations and/or surface/interfacial roughness. The Ir(001)/MgO(001) layer series deposited at $T_s = 1000$ °C is likely the most representative to quantify the intrinsic Ir resistivity scaling, due to its high crystalline quality and small surface roughness which are nearly thickness-independent for $d \geq 19.5$ nm. The measured $\rho_o\lambda_{eff} = (3.8 \pm 0.6)\times10^{-16}$ Ωm^2 from this series is quite small. It is 1.7, 2.6, 3.2,1.3, and 1.2 times smaller than the reported values for competing interconnect materials including Cu, W, Co, Ru, and Rh, respectively, indicating great promise for Ir as an alternate metal in narrow high conductivity interconnects.

Supplementary Material

Supplementary Material to this paper includes XRD data from an as-deposited Ir layer with $T_s = 700$ °C, and SEM micrographs and EBSD maps from multiple samples discussed in Section III.

ACKNOWLEDGEMENTS

The authors acknowledge funding from SRC under task 2881, the NY State Empire State Development's Division of Science, Technology, and Innovation (NYSTAR) through Focus Center-NY–RPI Contract C150117, and the NSF under grant No. 1712752.

Data availability

The data that support the findings of this study are available within this article.

REFERENCES

[1] J.J. Plombon, E. Andideh, V.M. Dubin, and J. Maiz, Appl. Phys. Lett. **89**, 113124 (2006).
[2] K. Barmak, A. Darbal, K.J. Ganesh, P.J. Ferreira, J.M. Rickman, T. Sun, B. Yao, A.P. Warren, and K.R. Coffey, J. Vac. Sci. Technol. A Vacuum, Surfaces, Film. **32**, 061503 (2014).
[3] T.S. Kuan, C.K. Inoki, G.S. Oehrlein, K. Rose, Y. –P. Zhao, G. –C. Wang, S.M. Rossnagel, and C. Cabral, MRS Proc. **612**, D7.1.1 (2000).
[4] S.M. Rossnagel and T.S. Kuan, J. Vac. Sci. Technol. B Microelectron. Nanom. Struct. **22**, 240 (2004).
[5] D. Josell, S.H. Brongersma, and Z. Tőkei, Annu. Rev. Mater. Res. **39**, 231 (2009).
[6] Y. Ke, F. Zahid, V. Timoshevskii, K. Xia, D. Gall, and H. Guo, Phys. Rev. B **79**, 155406 (2009).
[7] J.M. Purswani and D. Gall, Thin Solid Films **516**, 465 (2007).
[8] J.S. Chawla and D. Gall, Appl. Phys. Lett. **94**, 252101 (2009).
[9] E. Milosevic, S. Kerdsongpanya, and D. Gall, in *2018 IEEE Nanotechnol. Symp.* (IEEE, 2018), pp. 1–5.
[10] X.-G. Zhang and W.H. Butler, Phys. Rev. B **51**, 10085 (1995).
[11] M. César, D. Gall, and H. Guo, Phys. Rev. Appl. **5**, 054018 (2016).
[12] J.S. Chawla, F. Gstrein, K.P. O'Brien, J.S. Clarke, and D. Gall, Phys. Rev. B **84**, 235423 (2011).
[13] J.S. Chawla and D. Gall, J. Appl. Phys. **111**, 043708 (2012).
[14] P.Y. Zheng, R.P. Deng, and D. Gall, Appl. Phys. Lett. **105**, 131603 (2014).
[15] S. Dutta, K. Sankaran, K. Moors, G. Pourtois, S. Van Elshocht, J. Bömmels, W. Vandervorst, Z. Tőkei, and C. Adelmann, J. Appl. Phys. **122**, 025107 (2017).
[16] M. César, D. Liu, D. Gall, and H. Guo, Phys. Rev. Appl. **2**, 044007 (2014).
[17] V. Timoshevskii, Y. Ke, H. Guo, and D. Gall, J. Appl. Phys. **103**, 113705 (2008).
[18] J.S. Chawla, F. Zahid, H. Guo, and D. Gall, Appl. Phys. Lett. **97**, 132106 (2010).
[19] F. Zahid, Y. Ke, D. Gall, and H. Guo, Phys. Rev. B **81**, 045406 (2010).
[20] E. Milosevic and D. Gall, IEEE Trans. Electron Devices **66**, 2692 (2019).
[21] E. Milosevic and D. Gall, AIP Adv. **10**, 055213 (2020).
[22] T.-H. Kim, X.-G. Zhang, D.M. Nicholson, B.M. Evans, N.S. Kulkarni, B. Radhakrishnan, E.A. Kenik, and A.-P. Li, Nano Lett. **10**, 3096 (2010).
[23] J.M. Rickman and K. Barmak, J. Appl. Phys. **114**, 133703 (2013).
[24] L. Lu, Y. Shen, X. Chen, L. Qian, and K. Lu, Science (80-.). **304**, 422 (2004).
[25] T. Zhou, N.A. Lanzillo, P. Bhosale, D. Gall, and R. Quon, AIP Adv. **8**, 055127 (2018).
[26] K. Fuchs, Math. Proc. Cambridge Philos. Soc. **34**, 100 (1938).
[27] E.H. Sondheimer, Adv. Phys. **1**, 1 (1952).
[28] A.F. Mayadas and M. Shatzkes, Phys. Rev. B **1**, 1382 (1970).
[29] D.K.C. Macdonald and K. Sarginson, Proc. R. Soc. London. Ser. A. Math. Phys. Sci. **203**, 223 (1950).
[30] T. Zhou and D. Gall, Phys. Rev. B **97**, 165406 (2018).
[31] N. Trivedi and N.W. Ashcroft, Phys. Rev. B **38**, 12298 (1988).
[32] Z. Tešanović, M. V. Jarić, and S. Maekawa, Phys. Rev. Lett. **57**, 2760 (1986).
[33] G. Fishman and D. Calecki, Phys. Rev. B **43**, 11581 (1991).
[34] P.Y. Zheng, T. Zhou, B.J. Engler, J.S. Chawla, R. Hull, and D. Gall, J. Appl. Phys. **122**, 095304 (2017).
[35] Y.P. Timalsina, A. Horning, R.F. Spivey, K.M. Lewis, T.-S. Kuan, G.-C. Wang, and T.-M. Lu,

Nanotechnology **26**, 075704 (2015).
[36] D. Choi, X. Liu, P.K. Schelling, K.R. Coffey, and K. Barmak, J. Appl. Phys. **115**, 104308 (2014).
[37] E. Milosevic, S. Kerdsongpanya, M.E. McGahay, A. Zangiabadi, K. Barmak, and D. Gall, J. Appl. Phys. **125**, 245105 (2019).
[38] D. Gall, J. Appl. Phys. **127**, 050901 (2020).
[39] D. Gall, J. Appl. Phys. **119**, 085101 (2016).
[40] C. Adelmann, K. Sankaran, S. Dutta, A. Gupta, S. Kundu, G. Jamieson, K. Moors, N. Pinna, I. Ciofi, S. Van Eishocht, J. Bommels, G. Boccardi, C.J. Wilson, G. Pourtois, and Z. Tokei, in *2018 IEEE Int. Interconnect Technol. Conf.* (IEEE, 2018), pp. 154–156.
[41] D. Gall, A. Jog, and T. Zhou, in *2020 IEEE Int. Electron Devices Meet.* (IEEE, 2020), pp. 32.3.1-32.3.4.
[42] E. Milosevic, S. Kerdsongpanya, A. Zangiabadi, K. Barmak, K.R. Coffey, and D. Gall, J. Appl. Phys. **124**, 165105 (2018).
[43] S.S. Ezzat, P.D. Mani, A. Khaniya, W. Kaden, D. Gall, K. Barmak, and K.R. Coffey, J. Vac. Sci. Technol. A **37**, 031516 (2019).
[44] A. Jog, T. Zhou, and D. Gall, IEEE Trans. Electron Devices **68**, 257 (2021).
[45] P. Zheng and D. Gall, J. Appl. Phys. **122**, 135301 (2017).
[46] E. Milosevic, S. Kerdsongpanya, M.E. McGahay, B. Wang, and D. Gall, IEEE Trans. Electron Devices **66**, 3473 (2019).
[47] E. Milosevic, P. Zheng, and D. Gall, IEEE Trans. Electron Devices **66**, 4326 (2019).
[48] P. Fang, B. Wang, and D. Gall, Surf. Coatings Technol. **420**, 127333 (2021).
[49] L. Trupina, L. Nedelcu, M.G. Banciu, A. Crunteanu, L. Huitema, C. Constantinescu, and A. Boulle, J. Mater. Sci. **55**, 1753 (2020).
[50] K. Klyukin, A. Zagalskaya, and V. Alexandrov, J. Phys. Chem. C **122**, 29350 (2018).
[51] P. Zheng, B.D. Ozsdolay, and D. Gall, J. Vac. Sci. Technol. A Vacuum, Surfaces, Film. **33**, 061505 (2015).
[52] J. Ye and C. V. Thompson, Appl. Phys. Lett. **97**, 071904 (2010).
[53] G.K. White and S.B. Woods, Philos. Trans. R. Soc. A Math. Phys. Eng. Sci. **251**, 273 (1959).
[54] T. Zhou, P. Zheng, S.C. Pandey, R. Sundararaman, and D. Gall, J. Appl. Phys. **123**, 155107 (2018).
[55] T. Sun, B. Yao, A.P. Warren, K. Barmak, M.F. Toney, R.E. Peale, and K.R. Coffey, Phys. Rev. B - Condens. Matter Mater. Phys. **81**, 1 (2010).
[56] N.A. Lanzillo, J. Appl. Phys. **121**, 175104 (2017).
[57] N.A. Lanzillo, P. Bhosale, C. Lavoie, D.J. Dechene, R.R. Robison, and K. Choi, J. Phys. D. Appl. Phys. **52**, (2019).

Preprint, published as: Atharv Jog and Daniel Gall, "Resistivity size effect in epitaxial iridium layers," J. Appl. Phys. **130**, 115103 (2021); https://doi.org/10.1063/5.0060845

Figures

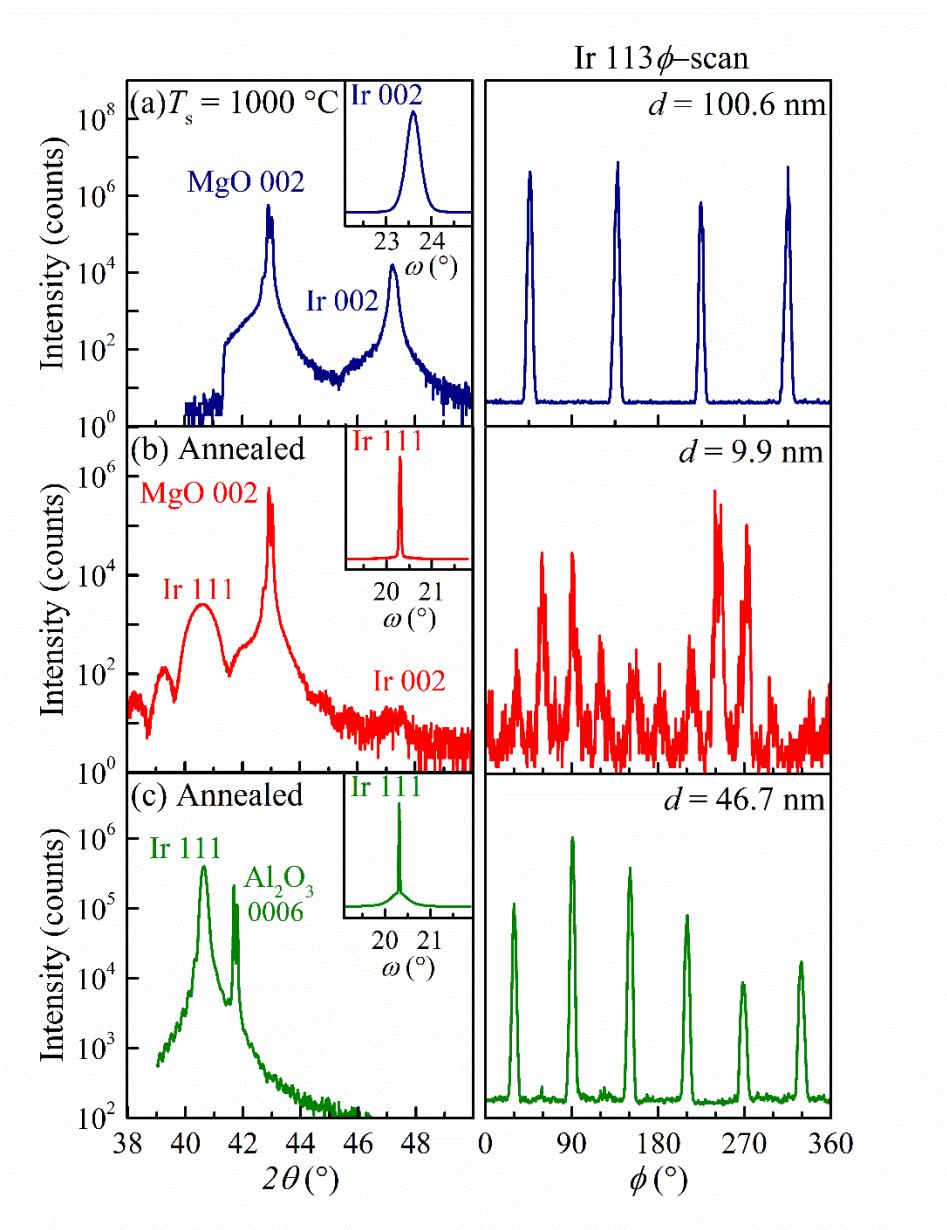

Figure 1. Representative XRD θ-2θ scans, ω-rocking curves from the primary Ir reflection (insets), and Ir 113 ϕ-scans from (a) an Ir(001)/MgO(001) layer grown at T_s = 1000 °C with d = 100.6 nm (b) a multi-domain d = 9.9 nm Ir/MgO(001) layer grown at T_s = 700 °C and annealed to 1000 °C, and (c) an Ir(111)/Al_2O_3(0001) layer with d = 46.7 nm.

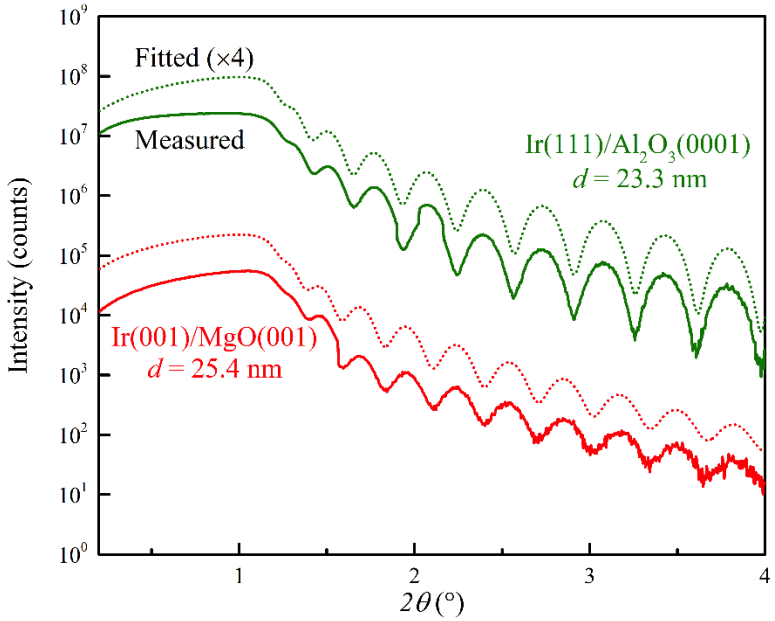

Figure 2. X-ray reflectivity curves for an Ir(111)/Al_2O_3(0001) (green) and an Ir(001)/MgO(001) (red) layer. Solid lines are the measured intensity and dotted lines are results from curve fitting.

Preprint, published as: Atharv Jog and Daniel Gall, "Resistivity size effect in epitaxial iridium layers," J. Appl. Phys. **130**, 115103 (2021); https://doi.org/10.1063/5.0060845

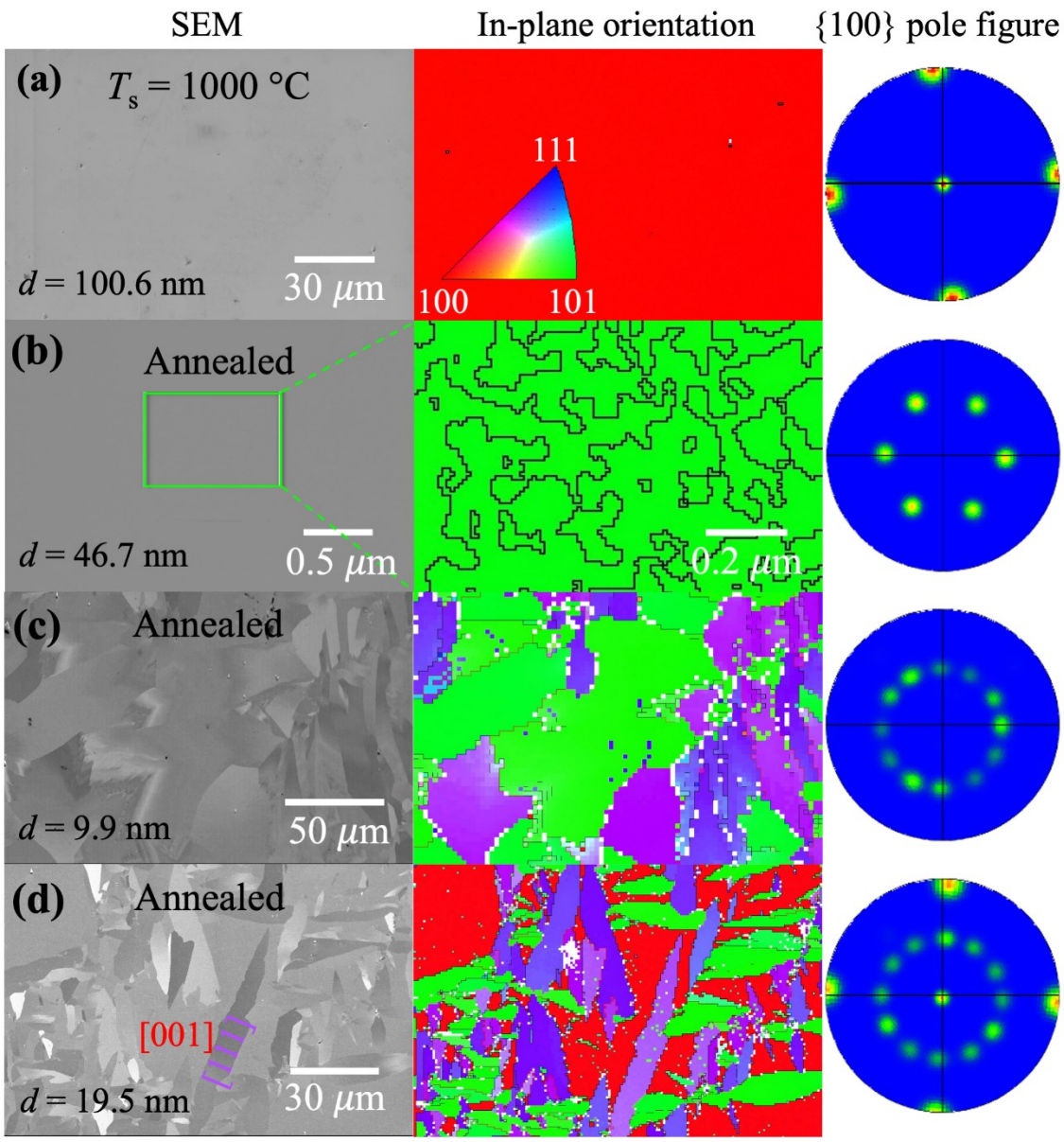

Figure 3. SEM micrographs, in-plane orientation maps, and corresponding Ir{100} EBSD pole figures for Ir layers on (a) MgO(001) with d = 100.6 nm and T_s = 1000 °C , (b) Al_2O_3(0001) with d = 46.7 nm and T_s = 700 °C and annealed, (c) MgO(001) with d = 9.9 nm and T_s = 700 °C and annealed, and (d) MgO(001) with d = 19.5 nm and T_s = 700 °C and annealed.

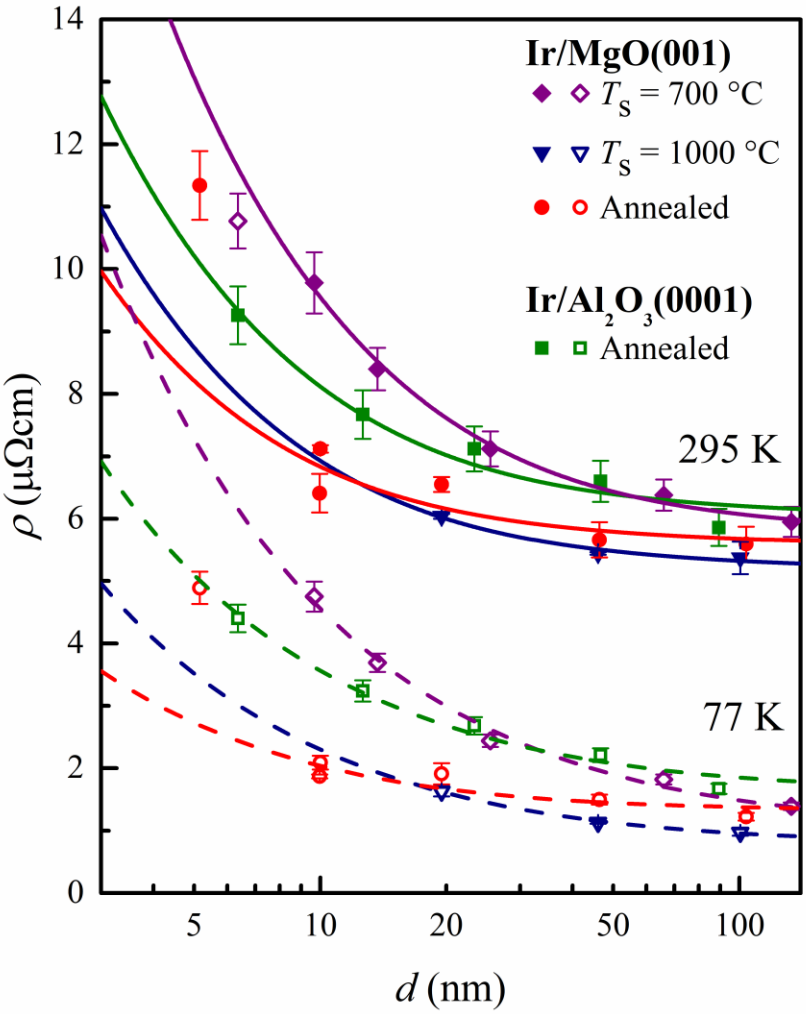

Figure 4. Resistivity ρ vs thickness d at 295 and 77 K (solid and open symbols, respectively) from epitaxial Ir deposited on MgO(001) at T_s = 1000 °C (blue triangles), 700 °C (purple diamonds), and 700 °C followed by *in situ* annealing (red circles), and two-domain Ir(111)/Al_2O_3(0001) layers (green squares). Lines are the result from curve fitting using the FS and MS models.

T_s (°C)	Thickness d (nm)	Roughness σ (nm)	ρ (μΩcm)		
			295 K		77 K
			In situ	*Ex situ*	
1000	7.7	1.1	$>10^6$	$>10^6$	$>10^6$
	11.5	0.87	18.7 ± 0.2	18.9 ± 0.3	7.4 ± 0.3
	19.5	0.41	6.04 ± 0.04	6.10 ± 0.05	1.63 ± 0.08
	46.0	0.43	5.44 ± 0.02	5.49 ± 0.09	1.13 ± 0.02
	100.6	0.53	5.37 ± 0.26	5.38 ± 0.27	0.97 ± 0.05
700	6.8	0.36	14.2 ± 0.5	14.4 ± 0.6	10.8 ± 0.4
	9.6	0.46	9.78 ± 0.49	10.08 ± 0.50	4.75 ± 0.24
	13.7	0.23	8.40 ± 0.34	8.55 ± 0.35	3.69 ± 0.14
	25.4	0.33	7.12 ± 0.28	7.29 ± 0.30	2.44 ± 0.10
	66.1	0.1	6.38 ± 0.25	6.46 ± 0.26	1.82 ± 0.08
	133.1	-	5.95 ± 0.24	5.95 ± 0.24	1.39 ± 0.06
700 +Anneal (1000 °C)	5.2	0.23	11.3 ± 0.5	12.9 ± 0.3	4.9 ± 0.3
	9.9	0.16	6.41 ± 0.31	6.70 ± 0.09	1.87 ± 0.03
	10.0	0.22	7.12 ± 0.06	7.42 ± 0.08	2.09 ± 0.11
	19.5	0.39	6.55 ± 0.12	6.70 ± 0.61	1.91 ± 0.17
	46.4	0.18	5.66 ± 0.29	5.97 ± 0.30	1.50 ± 0.08
	103.9	0.34	5.59 ± 0.28	5.89 ± 0.29	1.22 ± 0.06

Table 1. Thickness, root-mean-square surface roughness, and resistivity measured *in situ* and *ex situ* at 295 K and immersed in liquid nitrogen at 77 K, of epitaxial Ir layers grown on MgO(001) substrates at T_s = 1000 °C, 700 °C, and 700 °C followed by *in situ* step-wise annealing to 1000 °C.

T_s (°C)	Thickness d (nm)	Roughness σ (nm)	ρ (μΩcm)		
			295 K		77 K
			In situ	*Ex situ*	
700 +Anneal (1000 °C)	6.4	0.32	9.26 ± 0.46	9.55 ± 0.48	4.40 ± 0.22
	12.6	0.46	7.67 ± 0.39	7.73 ± 0.40	3.24 ± 0.17
	23.3	0.32	7.12 ± 0.36	7.25 ± 0.37	2.68 ± 0.14
	46.7	0.28	6.60 ± 0.33	6.61 ± 0.33	2.21 ± 0.11
	89.3	0.24	5.86 ± 0.30	5.99 ± 0.30	1.67 ± 0.08

Table 2. Thickness, root-mean-square surface roughness, and resistivity measured *in situ* and *ex situ* at 295 K and immersed in liquid nitrogen at 77 K of two-domain epitaxial Ir(111)/Al_2O_3(0001) layers grown at T_s = 700 °C followed by *in situ* annealing.

Sample Series	λ_{eff} (nm) 295 K	λ_{eff} (nm) 77 K	$\rho_o\lambda_{eff}$ (10^{-16} Ωm^2) 295 K	$\rho_o\lambda_{eff}$ (10^{-16} Ωm^2) 77 K
700 °C	14.3 ± 0.8	83 ± 16	8.2 ± 0.4	8.9 ± 1.8
1000 °C	7.4 ± 1.2	43.8 ± 5.2	3.8 ± 0.6	3.5 ± 0.4
700 °C + annealed	5.1 ± 1.8	11.8 ± 4.8	2.8 ± 1.0	1.5 ± 0.6
Substrate: Al_2O_3	8.8 ± 0.9	58.6 ± 5.5	4.5 ± 0.5	4.7 ± 0.4

Table 3. Effective bulk electron mean path λ_{eff} and corresponding $\rho_o\lambda_{eff}$ product at 295 and 77 K from epitaxial Ir deposited on MgO(001) at T_s = 1000 °C, 700 °C, and 700 °C followed by *in situ* annealing, and from two-domain Ir(111)/Al_2O_3(0001) layers.

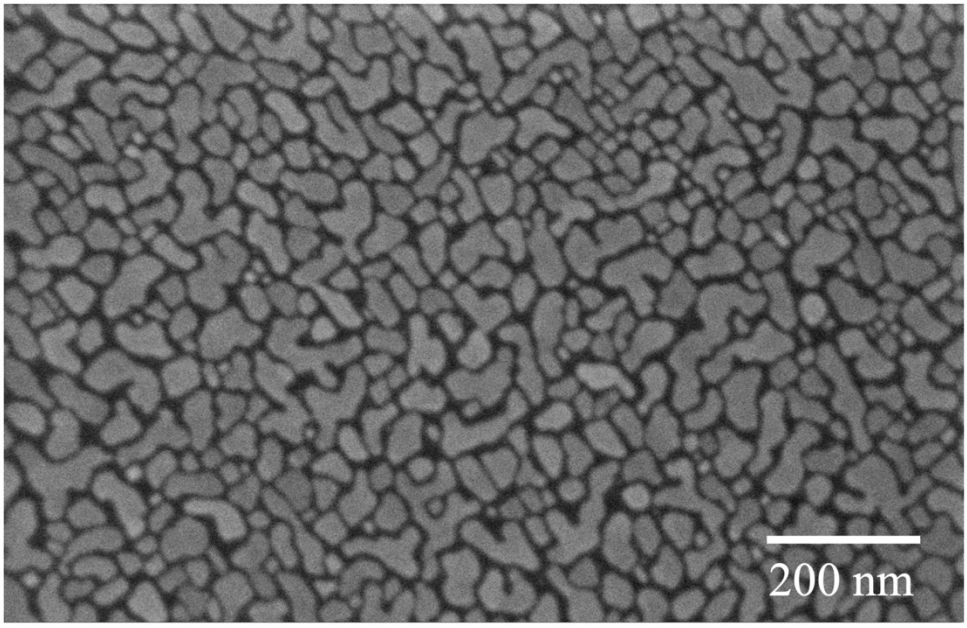

Supplementary Figure S1. Scanning electron micrograph from a 7.7-nm-thick Ir layer grown on MgO(001) at T_s = 1000 °C. The bright areas in the micrograph are Ir islands which are separated by trenches, suggesting that this Ir layer has not coalesced and thus explains the infinitely high measured resistivity for this layer with d = 7.7 nm.

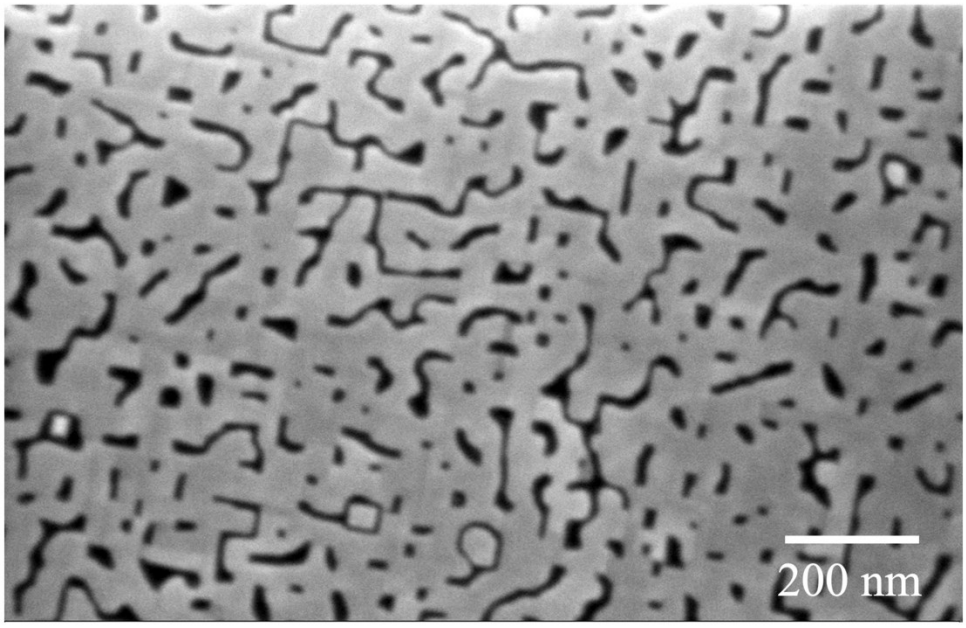

Supplementary Figure S2. Scanning electron micrograph from a 11.5-nm-thick Ir layer grown on MgO(001) at T_s = 1000 °C. The dark areas in the micrograph are holes, indicating partial surface coverage caused by lack of film closure, which explains high resistivity observed for this layer.

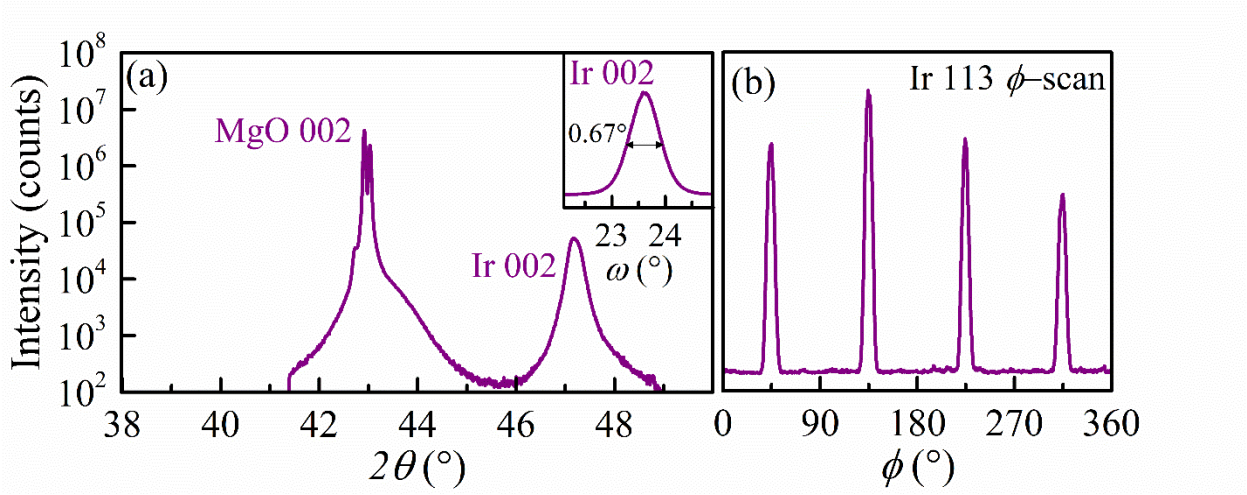

Supplementary Figure S3. (a) θ-2θ scan with ω-rocking curve of Ir 002 reflection in the inset and (b) Ir 113 ϕ-scan from a Ir(001)/MgO(001) layer grown at T_s = 700 °C with d = 66.1 nm. The combination of x-ray diffraction analyses demonstrates a cube-on-cube epitaxial growth of Ir(001) on MgO(001).

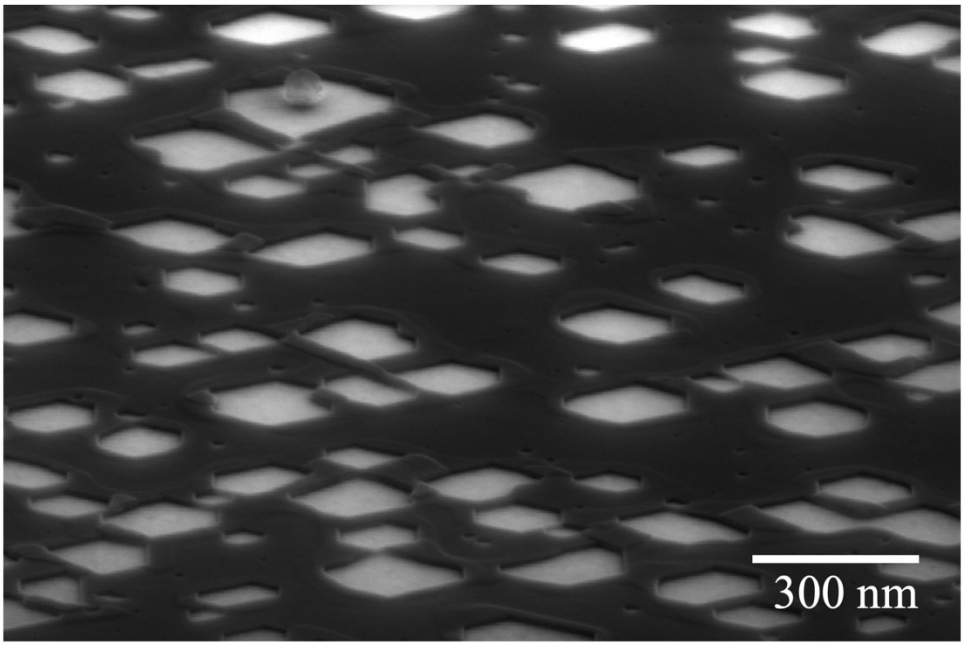

Supplementary Figure S4. Scanning electron micrograph from a 5.2 -nm-thick Ir layer grown on MgO(001) at T_s = 700 °C followed by *in situ* annealing. The bright areas in the micrograph are holes, indicating only partial surface coverage caused by dewetting, resulting in an increased resistivity.

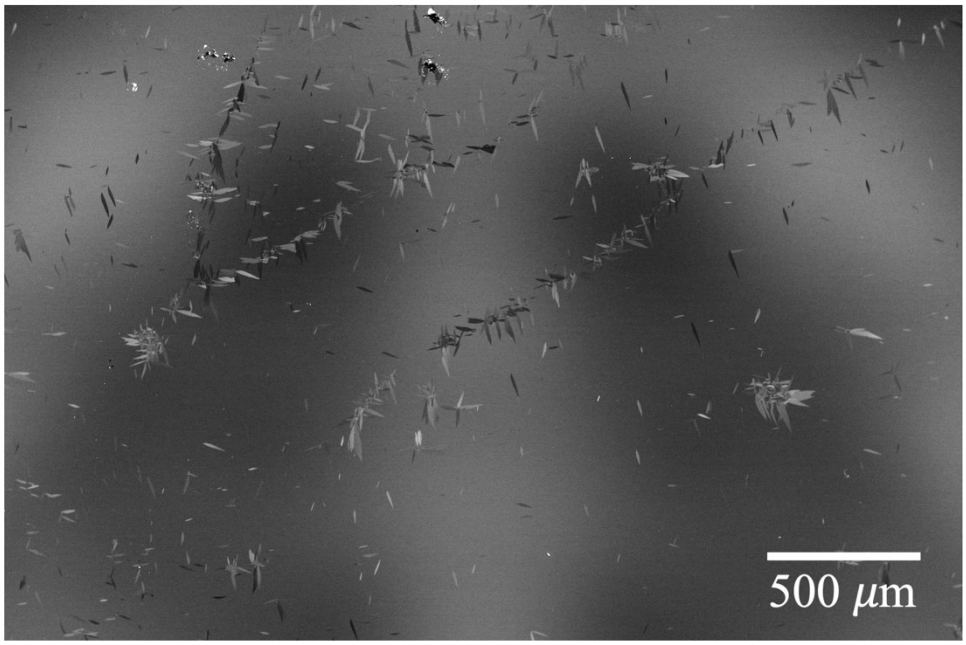

Supplementary Figure S5. Low-magnification scanning electron micrograph from a 19.5-nm-thick Ir layer grown on MgO(001) at T_s = 700 °C followed by in situ annealing. The elongated grains are renucleated 111-domains while the majority of the layer remains an epitaxial Ir(001) layer. The mixed domain microstructure and particularly the residual Ir(001) results in an elevated resistivity.

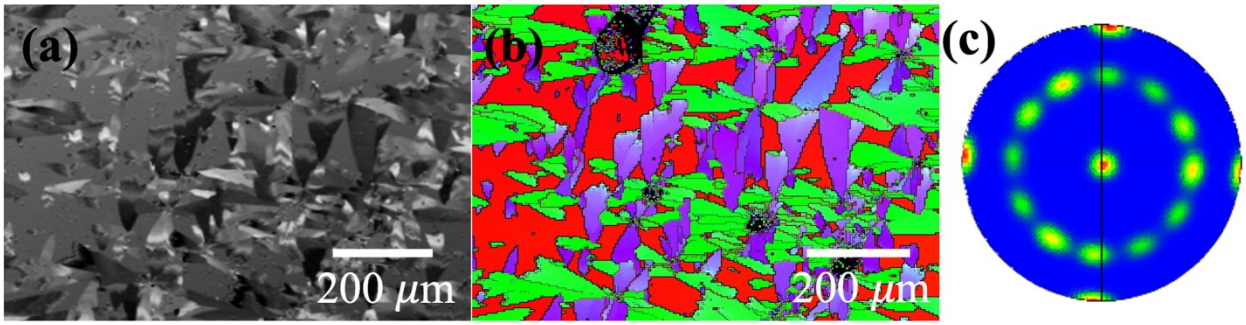

Supplementary Figure S6. (a) SEM micrograph, (b) in-plane orientation map, and (c) corresponding Ir{100} EBSD pole figure from an Ir/MgO(001) layer with d = 10.0 nm and T_s = 700 °C followed by *in situ* annealing. The in-plane orientation map shows a considerable fraction of residual Ir 001-domains. This fraction is larger than for a nominally identical layer with d = 9.9 nm. The higher fraction of residual Ir 001-domains is attributed to the stochastic renucleation process and explains the higher resistivity of this layer despite the same nominal thickness.

This EBSD analysis of the d = 10.0 nm layer shows a microstructure comparable to the d = 19.5 nm layer presented in Fig. 3(d) in the main text. The micrograph suggests large renucleated 111-domains which are indicated by purple, violet, and green colors in the corresponding in-plane orientation map. The {100} pole figure exhibits a central spot from the residual 001-oriented part of the layer while the four-distinct 90° in-plane rotated domains give rise to twelve poles.